This article appeared in The Journal of Chemical Physics 164, 144911 (2026) and may be found at https://doi.org/10.1063/5.0306965

Characterization of Dynamics of Encapsulated Small Molecule Nile Red in Biodegradable Polymer using 2D IR Methods

Anneka Miller Casas, Victor Wen, Nehal S. Idris, Joseph P. Patterson, Nien-Hui Ge*
Department of Chemistry, University of California, Irvine, CA 92697-2025

*To whom correspondence should be addressed: nhge@uci.edu

Abstract

Biodegradable polymers are seen as a promising option for drug delivery. Here we applied 2D IR methods with scattering removal to characterize the vibrational dynamics of encapsuled Nile red in amphiphilic block copolymer polyethylene glycol-*block*-polycaprolatone. Nile red was chosen because it is a commonly used hydrophobic dye molecule. Comparing the absorptive spectra, the splitting of diagonal peaks in nonrephasing spectra confirms the encapsulation of Nile red in the presence of polymer droplets. Pump–probe lifetime data exhibit multiple exponential decays and oscillations, which were fitted to quantify the encapsulation. Waiting time dependent 2D IR spectra were acquired and simulated to characterize the dynamics of the encapsulated Nile red. From these results, we can determine that a portion of the Nile red population, in the presence of polymer, exhibits distinctly different vibrational dynamics, consistent with encapsulation within coacervate microdroplets.

Introduction

Plastics are ubiquitous in modern life. Broadly, researchers are interested in biodegradable polymers for plastics, agriculture, and packaging. Approximately 275×10^6 metric tons of plastic waste was generated in 2010 alone.[1] Biodegradable materials which can replace these plastics may significantly reduce the myriad problems associated with this enormous use of plastics including plastic waste found in the ocean,[1] drinking water,[2] and food.[3] Amphiphilic block copolymers are considered biodegradable due to their cleavable ester linkages.[4] This has led researchers to consider them for applications in plastics,

agriculture, packaging, and drug delivery.[4,5] Researchers have been interested in biodegradable polymers for drug-delivery since at least the 1970s.[5]

When considering the different uses for biodegradable polymers in drug delivery, characterizing the encapsulation of small molecules may be useful for determining which polymers may work well with particular drugs. Nile red, shown in Figure 1 (a), is a commonly used hydrophobic small molecule dye. Due to its fluorescence, it has been used to stain lipids,[6,7] assess cyclodextrins,[8,9] and study polymeric nanoparticles[10,11] and micelles.[12-14] We used this small-molecule model to characterize the efficacy of nonionic amphiphilic block copolymer polyethylene glycol-*block*-polycaprolactone (PEG_{45}-*b*-PCL_{30}) for encapsulation of small molecules. We chose to start this project with this well-characterized small molecule so that we can someday expand this work to more complex systems, which lack fluorescence and, therefore, have hampered researchers' capacity to characterize encapsulation. We recently confirmed the encapsulation of Nile red in PEG_{45}-*b*-PCL_{30} coacervates.[15] Here we further assess the consistency in encapsulation and characterize the dynamics of the encapsulated Nile red. Two-dimensional infrared spectroscopy (2D IR) has been used to study molecular dynamics for the last two decades[16] since its invention.[17,18] It is a powerful technique that can be used to estimate the angle between transition dipole moments, which can be translated to estimate the angles between bonds,[16,19-21] and to investigate correlated vibrational motions,[22,23] and the dynamics of solutions[24-26] and solids.[27] 2D IR studies on polymer microdroplets have been hindered by significant scattering. Our recent development of the SEIFDA (Scattering Elimination Immune from Detector Artifacts) method which removes scattering exceedingly well for all polarizations[15] has enabled us to characterize the encapsulation of Nile red within PEG_{45}-*b*-PCL_{30} coacervates.

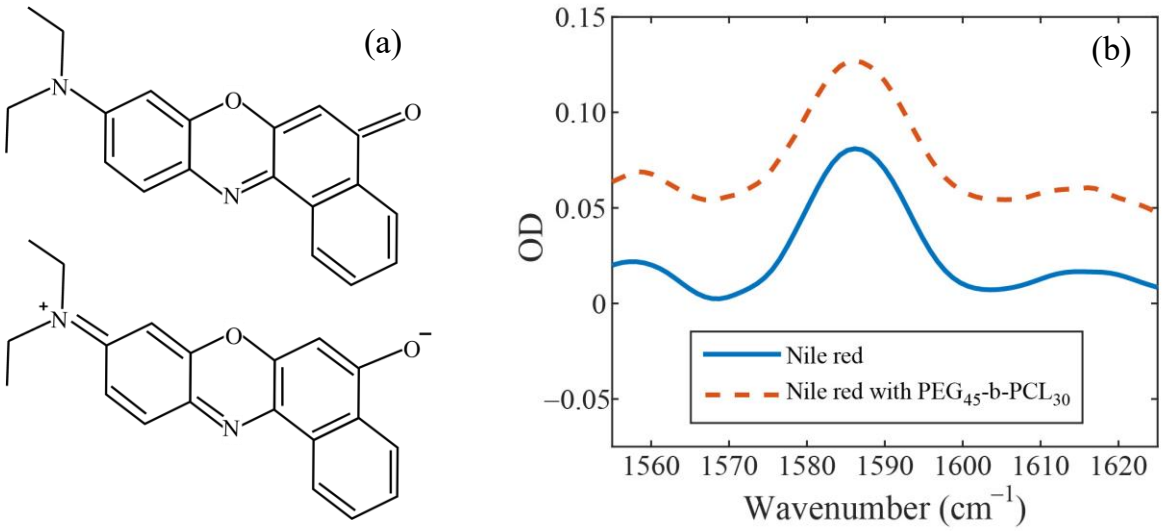

Figure 1: (a) Nile red resonance structures. (b) FTIR of Nile red with and without polymer PEG_{45}-*b*-PCL_{30} in 70% by volume dioxane and 30% D_2O.

Methods

Samples

Nile red samples were prepared in the same way as in our previous study.[15] For Nile red with polymer samples, 1.12 mM of polymer PEG_{45}-*b*-PCL_{30} was polymerized in 5 mM of Nile red in dioxane. This was then diluted with the addition of D_2O. The final Nile red concentration was 3.5 mM and the solvent was 70% dioxane and 30% D_2O by volume. The samples with unencapsulated Nile red were prepared by preparing 5 mM Nile red in dioxane, then adding D_2O until the final solution was 70% dioxane and 30% D_2O by volume with 3.5 mM Nile red. The solutions were vortexed for ~ 25 s before they were pipetted into a sample cell. The diameters of the droplets were between 10 and 20 μm, as estimated using optical confocal microscopy.[28] To confirm that there is no aggregation of Nile red at the concentration used, FTIR spectra were measured in a series of samples with 0.70, 1.4, 2.1, 2.8, and 3.5 mM Nile red in 70% dioxane and 30% D_2O, by volume. After accounting for small variations in sample cell thickness and

dividing the spectra by the concentration, good overlap between these spectra was observed. For the samples without polymer, after ~5 days, the initial color of the solution would begin to fade. This has been attributed to the aggregation of Nile red.[9] No measurements were performed on the faded cells. No fading was observed for the samples with Nile red and polymer. However, these were refreshed as frequently as the Nile red in solvent samples to ensure consistency in case the unencapsulated Nile red was becoming aggregated.

Spectroscopy

We acquired all the linear IR spectra using a Jasco 4700 FTIR purged with dry air. Harrick cells with 100-μm Teflon spacers and CaF_2 windows were used. The solvent peaks (70% by volume dioxane and 30% D_2O) were removed by subtracting the solvent spectrum acquired immediately before using a thickness-matched spacer and cell.

We acquired 2D IR data in the pump–probe geometry using a setup previously described.[29] Time zero was found using a position on the sample cell with significant scattering. We scanned the time between the first and second pump pulse, τ, from 0 to 4.5 ps in 0.025 ps steps using an acousto-optic modulator-based home-built pulse shaper. The pump–probe delay time was set by a computer-controlled translation stage. The probe spectrum was calibrated using water lines. The pump spectrum was calibrated using neat acetone and a 100-μm thick sample of 5 mM benzanilide dissolved in dimethyl sulfoxide. The probe frequency, ω_t was directly reported by the spectrometer. The pump frequency, ω_τ, was obtained by Fourier transforming the time domain data along τ. The waiting time, T_w, was scanned using a delay stage in the probe path. The pump was s-polarized. When both ⟨YYZZ⟩ and ⟨ZZZZ⟩ were collected, at the sample, the probe was polarized at 45°to the table. After the sample, prior to detection, the ⟨YYZZ⟩ and ⟨ZZZZ⟩ were separated using an analyzer which allowed the s-polarized to pass and reflected the p-polarized. The p-polarized signal was then transmitted through another polarizer to clean the signal. When only ⟨ZZZZ⟩ spectra were collected, the λ/2 waveplate prior to the signal generation was used to change

the probe polarization to s. The MCT we use has 2 rows with 32 pixels in each row which allows us to detect ⟨YYZZ⟩ and ⟨ZZZZ⟩ simultaneously, when desired. Optimized referencing[30,31] was implemented using a separate reference array detector. Two consecutive blank shots were acquired at intervals spaced by 5% of the data to build the B matrix. This corresponded to once every 10 steps along τ (4 phases × 10 steps along τ = 40 shots). Scattering was effectively removed using SEIFDA.[15] This is possible because optimized referencing effectively reduces the effects of laser noise on the spectrum. However, SEIFDA may not be suitable for high intensity and tight focus environments where thermal grating may affect the scattering in a time dependent manner.[32]

When studying samples with polymer present, we confirmed that sufficient polymer droplets were in the focus first by observing strong Mie scattering, then by measuring the polymer ester carbonyl absorbance near 1717 cm^{-1}.

Computations

In order to assign modes, we performed Density Functional Theory (DFT) harmonic and anharmonic calculations at the B3LYP/6-311++g(d,p) level with implicit water solvent using Gaussian 16.[33]

Results

Linear IR and 2D IR spectroscopy and peak assignment

Figure 1(b) shows FTIR spectra of Nile red with and without polymer. The differences between these two samples are very subtle. Nile red without polymer interacts only with the dioxane–D_2O solvent and is unencapsulated. The sample with polymer contains both encapsulated and unencapsulated Nile red. Table 1 summarizes the FTIR peak frequencies of the Nile red without polymer sample and the DFT calculated anharmonic frequencies and IR intensities. The results from DFT calculations indicate that the mode centered at 1586 cm^{-1} in the FTIR acquired for Nile red in dioxane–D_2O solvent predominantly

comes from the C=O bond stretching but has contributions from the neighboring rings (Figure 1a top). The modes observed at 1557 and 1616 cm^{-1} in the FTIR predominantly come from the same ring motions, but they also have contributions from the C=O bond stretching. As these modes arise from the bending and stretching of many of the same bonds, we will refer to them as A, B, and C, for clarity, where A has the lowest and C has the highest frequency. Note that there are two modes contributing to B, which differ by less than 0.03 cm^{-1} and are composed of nearly the same molecular motions, so we will treat the two as degenerate.

Table 1: FTIR frequencies of Nile red in 70% dioxane and 30% D_2O without polymer. DFT calculated anharmonic frequencies and IR intensities of Nile red in implicit water.

Mode	Observed Frequency in FTIR (cm^{-1})	DFT Anharmonic Frequency (cm^{-1})	IR Intensity predicted by DFT (km/mol)
A	1557	1537.11	114.86
B	1586	1566.91/1566.94	250.92/1113.52
C	1616	1600.75	30.79

Comparing the absorptive 2D IR spectra in Figures 2 (a) and (e) does not immediately reveal much about the encapsulation of Nile red in the polymer droplets. However, when we utilize the Kramers-Kronig relation to extract the nonrephasing spectra,[34-36] we see that there are several peaks in the spectrum for Nile red with polymer (Figure 2(g)) that do not appear in the spectrum for Nile red without polymer (Figure 2(c)). Previous studies have shown that nonrephasing spectra have higher resolving power to reveal overlapping peaks than rephasing[22,37] and absorptive spectra.[38,39] By comparing the peak positions, we concluded that the brightest diagonal peak in Figure 2(g) based on integration across each peak, which is observed at (ω_τ, ω_t) = (1589, 1589) cm^{-1}, was most likely coming from the unencapsulated Nile red because this peak is quite close to the peak at (1585, 1585) cm^{-1} in Figure 2(c) when Nile red only interacts with solvent . The nearby peak observed at (1579, 1574) cm^{-1} is then assigned to encapsulated Nile red peak B. It appears that the lower frequency A is also split in the presence of polymer and one contribution now appears at (1558, 1559) cm^{-1} while the other appears at

(1566, 1565) cm^{-1}. A cross peak observed at (1558, 1574) cm^{-1} between the peak observed at (1558, 1559) cm^{-1} and the peak assigned to encapsulated Nile red mode B observed at observed at (1579, 1574) cm^{-1} suggests that the peak at (1558, 1559) cm^{-1} likely comes from the encapsulated Nile red mode A. This leaves the peak at (1566, 1565) cm^{-1} to the unencapsulated Nile red mode A. There is a weak cross-peak at (1596,1561) cm^{-1}, which may be challenging to interpret. To confirm the assignments, the spectra were simulated and the assignments of encapsulated mode A and unencapsulated mode A were tested. We discuss the simulation parameters later in the paper. The frequency of the cross peak, which most closely agreed with the data, confirmed the assignment of the lower frequency mode A to encapsulated Nile red and the higher frequency mode A to unencapsulated Nile red. This indicates that encapsulation decreases the frequencies of modes A and B. In Figure 2(g), there are three remaining peaks. One is observed at (1610, 1605) cm^{-1}, another at (1615, 1610) cm^{-1}, and the last at (1620, 1612) cm^{-1}. There is insufficient evidence to assign these three peaks from the nonrephasing spectrum alone. Due to the nodal lines perpendicular to the diagonal line, which lead to interference between closely spaced peaks,[22] absolute value nonrephasing spectra cannot be relied upon alone to determine frequency. Note that some parallel lines appear at around ω_t=1556 cm^{-1} in Figure 2(g). We think that this feature is likely to come from noise on the edge pixels, which is more evident in the nonrephasing spectra than in the absorptive spectra because nonrephasing spectra are typically broader and less intense than rephasing spectra in the presence of inhomogeneous broadening.

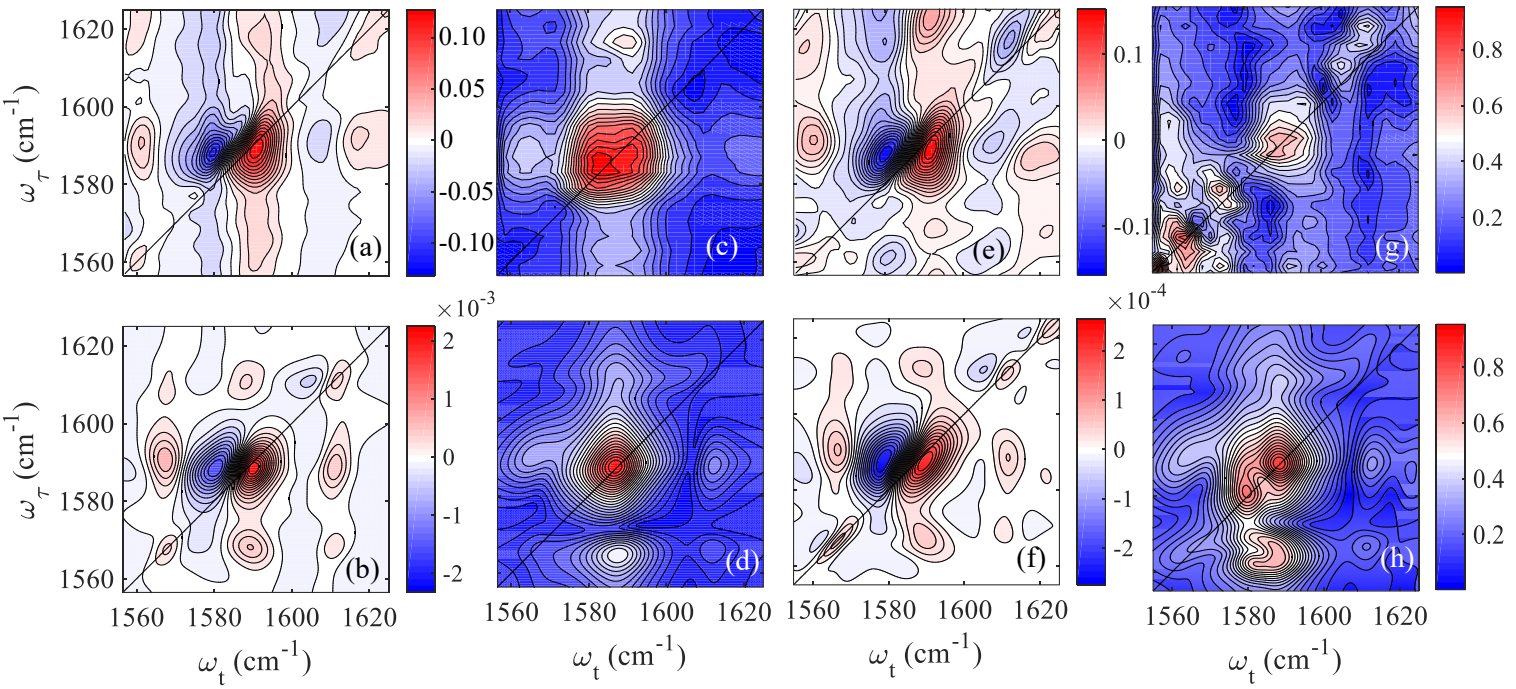

Figure 2: Experimental and simulated 2D IR spectra for unencapsulated Nile red in 70% dioxane and 30% D_2O (a)–(d) and for Nile red in dioxane–D_2O with PEG_{45}-*b*-PCL_{30} (e)–(h). (a) The absorptive spectrum for unencapsulated Nile red. T_w = 0 ps. (b) Simulation of unencapsulated Nile red. T_w = 0 ps. (c) Absolute value nonrephasing spectrum for unencapsulated Nile red extracted from the absorptive spectrum using the Kramers–Kronig relation. T_w = 0.3 ps (d) Simulation with T_w = 0.10 ps. (e) The absorptive spectrum for Nile red with polymer. T_w = 0.5 ps. (f) Simulation of encapsulated and unencapsulated Nile red. T_w = 0.5 ps (g) Absolute value nonrephasing spectrum for Nile red with polymer. T_w = 0.3 ps. (h) Simulation of encapsulated and unencapsulated Nile red. T_w = 0.1 ps. All with parallel polarization. See text for discussion of different waiting times used. Absorptive spectra are plotted using the same color bar as (a) and nonrephasing spectra are plotted as (g).

Lifetime Data

To estimate the ratio of unencapsulated to encapsulated Nile red within the focal volume, we performed pump–probe spectroscopy. The strong scattering was removed through phase cycling and subtraction of data acquired with a negative delay of 10 ps between the pump and probe.[15,40,41] Figure 3(a) and 3(e) show the pump–probe data across different frequencies at T_w = 0.44 ps for Nile red without and with polymer, respectively. The population relaxation dynamics for the ground state bleach of mode B at ω_t = 1591 cm^{-1} are shown in Figure 3(b) and 3(f). The isotropic signal was calculated using the parallel signal plus

two times the perpendicular signal. From the initial data that were taken with more sparse time points than those shown in Figure 3(b) and 3(f), we determined that the Nile red sample without polymer could be best fit using the sum of two exponential decays and the sample with Nile red and polymer could be best fit with three, based on the R^2 and the Akaike information criterion.[42,43] However, the lifetime data taken with more dense time points reveal an oscillatory feature in the lifetime data near 1.25 ps in Figure 3(b) and (f). This oscillatory feature could arise from Fermi resonance, anharmonic coupling, or overlapping peaks.[44,45] In addition to the two exponential decays used to describe the unencapsulated Nile red, a damped sine function was included, as shown in equation 1:[46]

$$P(T_{\mathrm{w}}) = a\,\mathrm{e}^{-\frac{T_{\mathrm{w}}}{\tau_1}} + b\,\mathrm{e}^{-\frac{T_{\mathrm{w}}}{\tau_2}} + c\,\mathrm{e}^{-\frac{T_{\mathrm{w}}}{\tau_d}} \sin\left(\frac{T_{\mathrm{w}}\pi}{\omega_d}\right) \quad (1)$$

where a and b are the coefficients, and τ_1 and τ_2 are the time constants of the two exponential decays, and the damped sine function has the coefficient c, time constant τ_d, and frequency ω_d. The exponential decay could not be accurately determined without including the damped sine function because the oscillatory feature would not be described otherwise. The fast and slow exponential decay time constants for the unencapsulated Nile red are 1.5 $\pm$ 0.2 and 7.8 $\pm$ 0.5 ps, respectively, and the ratio of the amplitude for the fast to the slow decay is 0.8 ± 0.1.

To determine the origin of the oscillatory feature, we removed the exponential decays from the dynamics, as shown in Figure 3(c), and Fourier transformed the residuals.[45] Although data were acquired out to 40 ps, we only included the data acquired between 0.45 and 8 ps in the Fourier transform of the residuals because the results are noisier when including data from delay times longer than the slowest decay time constants from fitting with equation 1. As shown in Figure 3(d), the most prominent peak after Fourier transforming the residuals is at $|\Delta\omega| = 27$ cm^{-1}, which is consistent with the frequency difference between mode B and mode A in the 2D IR absorptive spectra shown in Figure 2(a). Figure 2(a) confirms that this mode is coupled to mode B, as manifested in the cross peaks observed in the 2D IR at (1592,1560) and (1565,1592) cm^{-1}. The cross peaks at (1619,1591) and (1592,1617) cm^{-1} show that

mode B is also coupled to mode C. We attribute the weaker peak near $|\Delta\omega| = 31$ cm^{-1} in Figure 3(d) to this coupling. Figure 3(d) also shows the Fourier transform of the damped sine function obtained from fitting the time domain data in Figure 3(b), and the Fourier transform appears to fit the frequency domain well.

To fit the lifetime data of Nile red with polymer, we included three exponential decays and an additional damped sine function to account for the oscillations caused by the overlapping peaks from the encapsulated Nile red and unencapsulated Nile red, as shown in the following equation:

$$P(T_{\mathrm{w}}) = a\,\mathrm{e}^{-\frac{T_{\mathrm{w}}}{\tau_1}} + b\,\mathrm{e}^{-\frac{T_{\mathrm{w}}}{\tau_2}} + k\mathrm{e}^{-\frac{T_{\mathrm{w}}}{\tau_k}} + c\,\mathrm{e}^{-\frac{T_{\mathrm{w}}}{\tau_d}}\sin\left(\frac{T_{\mathrm{w}}\pi}{\omega_d}\right) + c_2\,\mathrm{e}^{-\frac{T_{\mathrm{w}}}{\tau_{d2}}}\sin\left(\frac{T_{\mathrm{w}}\pi-\varphi}{\omega_{d2}}\right) \qquad (2)$$

Here, the first two exponential decay time constants and their ratio were set to the same values as those of Nile red without polymer. These parameters describe the unencapsulated Nile red. The additional exponential decay constant τ_k and the amplitude k are for the encapsulated Nile red.

The first damped sine function in Eq. 2 was set to the same as that of Nile red without polymer. The second damped sine function in equation 2 has the coefficient c_2, time constant τ_{d2}, frequency ω_{d2}, and phase φ. For the unencapsulated Nile red, the phase appears to be 0. Simulations confirmed that the timing difference between the simulation (convolved with a Gaussian to account for the finite pulse width) and the data was minimized with the phase set to zero for the unencapsulated Nile red. We discuss the convolution of the simulation later in the paper, when we discuss the simulation. In contrast, the encapsulated and unencapsulated Nile red may have a phase difference. It seems reasonable to assume that this is a result of the physical separation between the origin of these signals and, therefore, the phase difference is due to an optical path length difference.

We initially allowed the three exponential time constants to freely vary to check whether they are consistent with the unencapsulated Nile red. We found good agreement between two of the three time constants for Nile red in solution with polymer and the two time constants for Nile red in solution without

polymer, confirming our assumption that these are coming from the unencapsulated Nile red in the sample. Although lifetime is commonly thought of as intrinsic, more recent studies have found that it is in fact subject to the Stark effect and that structure[47] and solvent reaction field[48] affect the vibrational lifetime. Amide I modes in particular have lifetimes that appear to depend upon hydration.[47] It seems reasonable that the mode studied here, predominantly coming from a C=O bond, may be dependent on hydration as well. Block copolymers made with hydrophilic PEG and hydrophobic PCL chains have been observed to form micelles,[49,50] vesicles,[51] and coacervates[28] in different solvent conditions. Because the encapsulated Nile red is expected to experience quite different local environments compared to the unencapsulated Nile red, it seems plausible that the electric fields surrounding the reporting group differ meaningfully, giving rise to a different vibrational lifetime. Note that we do not observe splitting of the encapsulated peak B at (1579, 1574) cm^{-1} in Figure 2(g), in contrast to the small splitting of the unencapsulated peak B at (1589, 1589) cm^{-1}; and a single decay constant of 8.3 ± 0.6 ps appears to describe the encapsulated lifetime data. We will discuss the splitting of unencapsulated peak B later in the paper.

Using the relative magnitude of the exponential decay coefficients from the fitting, we determined that the percentage of encapsulated Nile red varies significantly across the sample. The presence of encapsulated Nile red was confirmed using the Fourier transform of the residuals after removing the exponential decays. Figure 3(h) shows the result for the Nile red with polymer, which contains both encapsulated and unencapsulated, at ω_t=1591 cm^{-1}. At this wavelength, ~ 22.3% of the signal comes from the encapsulated Nile red. In addition to the peaks observed for unencapsulated Nile red in Figure 3(d), there is a prominent peak at 4–6 cm^{-1}. We attribute this peak to the frequency shift of peak B when Nile red is encapsulated. From the nonrephasing spectra in Figure 2(g), we had already confirmed that encapsulation shifts the frequencies of modes A, B, and C. As a result, we see that the Fourier transform of the first damped sine function no longer fits the residuals for the peaks attributed to coupling as well as it did for Nile red without polymer. These peaks, observed between 20 and 33 cm^{-1}

also have greater widths in the presence of polymer compared to without. This is likely due to the overlap of the signal coming from encapsulated Nile red and unencapsulated Nile red. We considered adding a third damped sine function to better fit these but were concerned about overparameterizing the data and, therefore, chose not to.

This article appeared in The Journal of Chemical Physics 164, 144911 (2026) and may be found at https://doi.org/10.1063/5.0306965

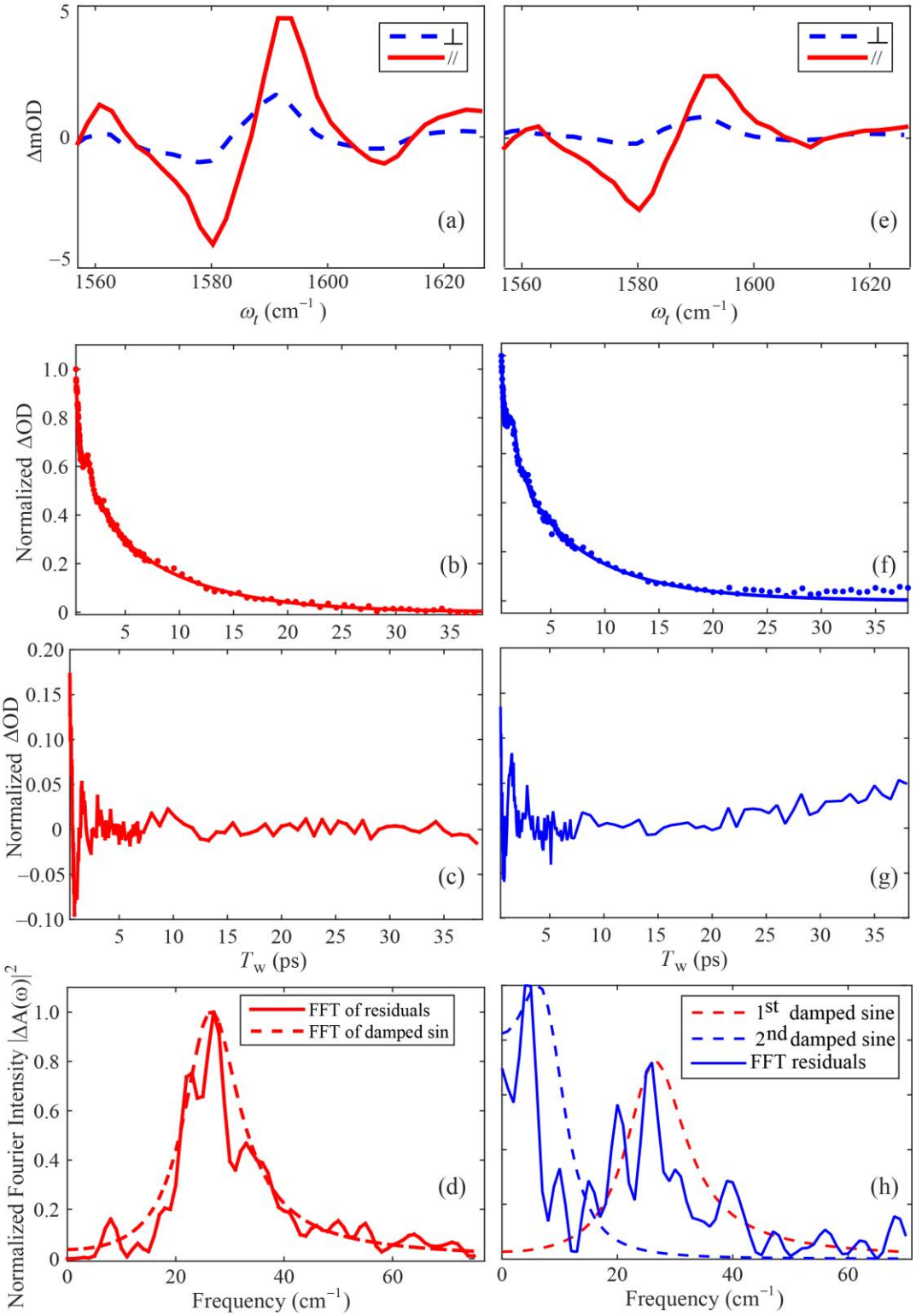

Figure 3: Lifetime dynamics, oscillations, and frequency components of mode B for Nile red in dioxane–D_2O without polymer (left column) and with polymer (right column). Panels in the first row, (a) and (e), are pump-probe data for a single waiting time, $T_w = 0.44$ ps. The next row shows the lifetime data calculated using the parallel plus two times the perpendicular spectra. The solid line in the Nile red without polymer is the biexponential fit with a damped sine function, using Eq. (1). The Nile red with PEG_{45}-*b*-PCL_{30} was fit using the same biexponential fit with a damped sine function plus an additional damped sine function and an exponential decay, using Eq. (2). The next row is the difference between the data points and the exponential fits (not including the damped sine functions). This reveals oscillatory features. The bottom row is the Fourier transform of the residuals in the above row. The dashed lines are the Fourier transforms of the damped sine function(s).

Characterizing Dynamics of Unencapsulated and Encapsulated Nile Red

Researchers use a plethora of methods to characterize the dynamics of 2D IR spectra including the nodal line slope,[23,52] the center line slope (CLS),[53] model fitting,[54] and dynamic mode decomposition.[55] However, these methods all have limited usefulness for coupled oscillators. To characterize the dynamics in this coupled oscillator system, we chose to simulate the spectra using the response functions.[22] However, it is challenging to confirm the consistency of a simulation with acquired data.[16,26] To validate our simulation, we utilized the CLS of the 0–1 transition for mode B, compared the simulated lifetime to acquired lifetime data, and compared the relative intensities of many of the peaks in 2D spectra. All peaks were compared to the intensity of the 0–1 transition for B, the brightest on the diagonal peak. The angles between the transition dipole moments were determined by comparing the cross-peak intensities for 2D IR spectra acquired with ⟨ZZZZ⟩ and ⟨YYZZ⟩.[56] Simulating the CLS of B was useful for directly determining many parameters including the dephasing time, Gaussian width and rate of spectral diffusion, and static inhomogeneity of B. In addition, the height of the oscillations observed in the CLS of B is sensitive not only to the dynamics parameters used for B but also to the terms used for A and C.

Because we do not have a system in which 100% of the sample is encapsulated, to characterize the encapsulated, we first must characterize the Nile red in solution without polymer, then determine how the spectra of the unencapsulated and encapsulated differ. It is reasonable to assume that the spectrum with unencapsulated and encapsulated will likely be the population-weighted sum of the unencapsulated and encapsulated. These spectra can be added because it is unlikely that there will be chemical exchange between the two populations within our experimental time scale.

Figure 4 shows the experimental and simulated linear IR, lifetime dynamics, and CLS for Nile red without polymer. The CLS of the 0–1 transition for mode B for unencapsulated Nile red, as shown in Figure 4(c), exhibits a very large oscillation. Figure 4(c) includes an exponential decay curve to help visualize the magnitude of the oscillations. To evaluate the source of this oscillation, we simulated the spectra using the response functions,[22] and the resulting CLS for the simulated spectra are shown in

Figure 4(d). From the simulation, we can conclude that much of the large oscillations in the CLS are likely due to the changes in the lineshape caused by coupling between A and B and between B and C. A and C are also coupled, but this is unlikely to change the line shape of B. These changes in line shape are caused by the overlap of features between the 0–1 transition for B and both the off- and on-diagonal cross peaks. From the simulation validated by the good agreement in CLS, we can extract many of the terms needed to describe the dynamics of the system. These are summarized in Table 2. The overlap between the cross-peaks and the 0–1 transition for B, makes the CLS of B sensitive to changes in the parameters input for peaks A and C as well, increasing our confidence in these values. The frequency-frequency correlation function (FFCF) we used for the i^{th} vibrator has the following form:

$$C_{ii}(t) = \frac{2\delta(t)}{T_{2,i}} + \sigma_{a,i}^2 e^{-t/\tau_{a,i}} + \sigma_{b,i}^2 \quad (1)$$

where $T_{2,i}$ is the dephasing time,[§] $\sigma_{b,i}$ is the static inhomogeneity, and $\sigma_{a,i}$ is the standard deviation of the Gaussian inhomogeneous distribution of the 0–1 transition that undergoes spectral diffusion. The response functions included the line shape functions, $g_{ii}(t)$, $g_{\Delta_i\Delta_i}(t)$, and $g_{ij}(t)$ corresponding to autocorrelation functions of 0−1 transition-frequency fluctuations, autocorrelation functions of diagonal-anharmonicity fluctuations, and cross-correlation functions of 0−1 transition frequency fluctuations, respectively.[22] The correlation between the fluctuations of the 1−2 and 0−1 transitions was ignored. The fluctuations of the diagonal anharmonicities were set to 0.5 cm^{-1} , about one tenth diagonal anharmonicities.[22] The cross-correlation functions included the spectral diffusion terms expressed as $c_{ij}\sigma_{a,i}\sigma_{a,j}e^{-t/\sqrt{\tau_{a,i}\tau_{a,j}}}$, where c_{ij} is the statistical correlation coefficient.

[§] See Ref. 57 for the factor of 2 in front of δ(t).

This article appeared in The Journal of Chemical Physics 164, 144911 (2026) and may be found at https://doi.org/10.1063/5.0306965

Table 2: Simulation parameters for Nile red in a solution of 70% dioxane and 30% D_2O (unencapsulated Nile red, abbreviated as Unencap.) and Nile red encapsulated in polymer microdroplets (abbreviated as Encap.) The parameters marked with * were set to the same values as those estimated for unencapsulated Nile red.

	Mode A		Mode B		Mode C	
	Unencap.	Encap.	Unencap.	Encap.	Unencap.	Encap.
$\omega_{0,i}$ (cm^{-1})	1568	1565	1589	1583	1611	1622
$T_{1,i}$ (ps)	7.77	7.77*	5.30	8.27	2.84	2.74
$T_{2,i}$ (ps)	0.63	0.45	1.36	1.75	0.98	0.90
$\sigma_{a,i}$ (cm^{-1})	3.50	2.50	6.35	10.0	3.00	2.50
$\tau_{a,i}$ (ps)	2.17	11.9	0.921	0.265	2.65	11.9
$\sigma_{b,i}$ (cm^{-1})	2.37	2.37*	1.91	0.751	0.751	0.751*

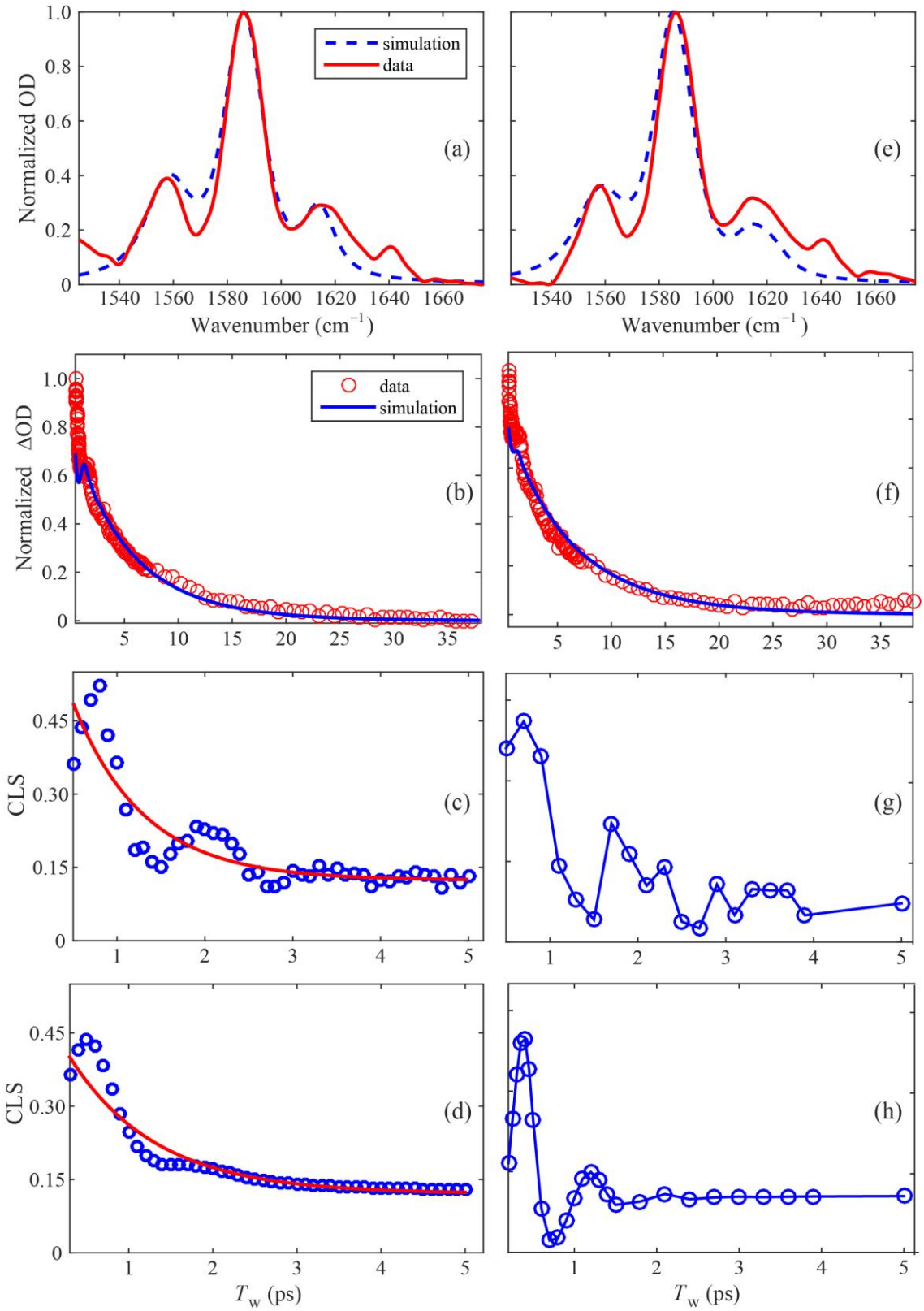

Figure 4: Experimental and simulation of Nile red in dioxane–D_2O without polymer (left column) and with polymer (right column). Overlaid acquired and simulated unencapsulated Nile red (a) linear IR and (b) lifetime. CLS for unencapsulated Nile red (c) acquired and (d) simulated. Overlaid acquired and simulated unencapsulated and encapsulated Nile red (e) linear IR and (f) lifetime. CLS for (g) extracted encapsulated Nile red from acquired data and (h) simulated encapsulated Nile red.

Comparing the simulated lifetime to the acquired lifetime data allowed us to better estimate the dephasing time. The results are shown in Figure 4(b). The apparent lifetime $T_{1,i}$ was determined based on when the data had decayed to 1/e the maximum intensity. The apparent $T_{1,i}$ was used because peaks A and B are both best fit to biexponential decays for the unencapsulated Nile red, which makes it challenging to accurately determine the vibrational lifetime. $T_{2,i}$ was first estimated from the CLS, then confirmed using the simulated linear IR spectrum as shown in Figure 4(a). There is an ~0.15–0.20 ps difference between the observed CLS maximum location in Figure 4(c) and the maximum location in the simulation in Figure 4(d). To try to recover this, a fourth peak observed at 1640 cm^{-1} in the FTIR in Figure 4(a) was added to the simulation. However, this addition did not reduce the timing difference and increased the computation time. Therefore, it was not included in the fittings shown in this section. This discrepancy in timing is similar to the finite pulse width in our setup, ~180 fs, and may be, in part, a result of this.

Simulated 2D absorptive spectra for unencapsulated Nile red are shown in Figure 2(b). The simulation recovers many of the features observed in the experimental spectrum in Figure 2(a), including the anticorrelation of the cross peak between A and B. This anticorrelation is likely caused by the prevalence of another resonance structure [Figure 1(a) bottom],[58] which changes the bond order of many of the bonds that contribute to both A and B.[39] The correlation coefficient, c_{ij}, of the two modes was set to −1 to recover the anticorrelation of this cross peak. To validate the simulation, we compared the CLS for mode B as well as the relative intensities of the diagonal and cross peaks. The angles between the transition dipole moments were determined by comparing the cross-peak intensity for spectra acquired with $T_w = 0$ ps with polarizations ⟨YYZZ⟩ and ⟨ZZZZ⟩, collected simultaneously using our dual-array detector.[56] The angles between A and B, A and C, and B and C, were determined to be 17.5°, 33.7°, and 25.2°, respectively.

Once the unencapsulated Nile red parameters were determined, we could fit the spectrum with polymer as the sum of the unencapsulated and encapsulated Nile red. To extract the CLS for the encapsulated Nile red, we used the CLS for the unencapsulated Nile red spectrum and the algorithm

proposed by Fenn and Fayer.[26] The percentage of the signal coming from encapsulated Nile red at each frequency was estimated using the lifetimes of the unencapsulated and encapsulated Nile red as well as the estimate for the frequency centers and Gaussian widths. These were estimated using a fit of the pump–probe spectra instead of the FTIR because the large focus spot in the FTIR made it impossible to estimate the percentage of encapsulated Nile red vs the percentage of unencapsulated. This percentage is not consistent across the sample because it depends on the amount of polymer droplets in a region of the sample cell. Furthermore, it seems to us that a fit of the lifetime data, which has the same dependence on the transition dipole as the 2D IR spectrum, would yield a more consistent lineshape than a fit of the FTIR.

Figure 4 shows the experimental and simulated linear IR, lifetime dynamics, and CLS for Nile red with polymer. The extracted and simulated CLS for the encapsulated are shown in Figure 4(g) and 4(h), respectively. Again, the CLS is highly oscillatory and, therefore, cannot be relied upon alone. However, comparing the CLS as well as the relative intensities of the diagonal and cross peaks gives us confidence that our simulation is capturing the dynamics from the spectra. The simulation recovers the oscillations in the CLS with very slightly different timing. The oscillations differ in location by ~0.15–0.20 ps, consistent with what we observed for the unencapsulated.

To confirm the parameters used for the lifetime of the encapsulated Nile red, we compared the lifetime data to the lifetime of the simulation. The results are shown in Figure 4(f). The simulation and the data are in very strong agreement. The oscillation observed at 1.25 ps in the data is observed at 1.20 ps in the simulation, after the simulation was convoluted with a Gaussian that represents our instrument response. This oscillation location depends primarily on the frequency differences between the oscillators in the system. Furthermore, the decays are in strong agreement.

The experimental 2D absorptive spectrum of Nile red with polymer is compared with the simulated spectrum in Figure 2(e) and 2(f). In order to confirm that there was significant PEG_{45}-*b*-PCL_{30} present in the focus, we first maximized scattering. Next, we confirmed the scattering was coming from

PEG_{45}-*b*-PCL_{30} using the polymer absorbance near 1717 cm^{-1}. In order to observe the Nile red peak as well as this peak, the mid-IR was tuned to a center near 1640 cm^{-1}. As a result, the peak near 1565 cm^{-1} was not always observed due to the limited light at this wavelength. This tradeoff seemed worth it, though, because it allowed us to confirm the presence of polymer droplets throughout the measurement. Figure 2(g) and 2(h) compare the acquired nonrephasing spectrum for Nile red with polymer and the population sum of the simulated unencapsulated and encapsulated Nile red. To obtain the nonrephasing spectrum, the simulated unencapsulated and encapsulated Nile red spectra were added in the time domain. Different waiting times were compared as the two-peak feature in nonrephasing spectra disappears in the simulation by 0.3 ps. At longer waiting times, the two-peak feature also disappears in the collected data. The timing discrepency was ~0.15–0.20 ps here as well, so T_w = 0.30 and 0.10 ps were, respectively, chosen for plotting the data and simulation in the figure.

The simulation parameters for encapsulated Nile red are summarized in Table 2 and indicate an increased lifetime and Gaussian linewidth for the brightest mode B compared to the unencapsulated Nile red. The differences observed in these parameters confirm that we are able to differentiate between the dynamics despite the significant spectral overlap. The increased lifetime in particular may indicate greater shielding from the solvent electric field.

The vibrational dynamics measured by 2D IR and simulated by the response functions is consistent with the picture that a portion of the Nile red population, in the presence of PEG_{45}-*b*-PCL_{30} in a 70:30 dioxane–D_2O mixture, is encapsulated by coacervate microdroplets, whereas the rest of the population is unencapsulated in the dilute phase. Prior studies on nonionic block copolymers showed that coacervates are formed when the hydrophobic blocks become sparingly soluble in solution.[59] Liquid–liquid phase separation gives rise to the dilute phase and the coacervate phase. The solvent composition in the dilute phase is expected to be similar to the pure solvent mixture because the volume of the coacervate phase is typically small, < 10% of the total volume, whereas the hydrophobic solvent is expected to be richer in the coacervate phase.[51] Indeed, the lifetime dynamics of the unencapsulated Nile red in the dilute

phase agree well with those in the pure solvent mixture. Because the coacervate phase is richer in dioxane than the dilute phase and the encapsulated Nile red is expected to experience less frequent hydrogen bond making-breaking with the solvent mixture as well as being shielded by the polymer, giving rise to a slower vibrational lifetime decay. Encapsulation of Nile red can occur in the hydrophobic region of the PEG_{45}-*b*-PCL_{30} or at the interface between the hydrophobic and hydrophilic regions of the polymer. Based on the computational predictions and experimental findings of a similar system,[60] we expect that Nile red is preferentially adsorbed at the interface because its concentration at 3.5 mM is lower than its solubility in 70:30 dioxane–D_2O as indicated by our concentration-dependent FTIR data. Cryo-TEM studies of PEG-*block*-poly methyl methacrylate (PEG_{45}-*b*-$PMMA_y$, y = 200 and 300) coacervate microdroplets revealed porous structures in the nanoscale.[28,61] We speculate that the PEG_{45}-*b*-PCL_{30} microdroplets studied in this paper may also have porous structures because both PEG_{45}-*b*-PCL_{30} and PEG_{45}-*b*-$PMMA_{170}$ in dioxane phase separate at 30% (v/v) H_2O and the Hildebrand and Hansen solubility parameters of PCL and PMMA are very similar.[28] Taking all together, we think that interfacial adsorption between the PEG and PCL domains is the dominant mechanism for Nile red encapsulation; and that these coacervate microdroplets exhibit internal nanoscale structures that can give rise to varied local environments with rich bath modes that are accessible by thermal fluctuations, such as CH_2 scissoring and ester carbonyl stretching modes.[62,63] These factors result in a larger Gaussian width and faster rate in the vibrational spectral diffusion dynamics of encapsulated Nile red, compared to unencapsulated Nile red.

One aspect not recovered in the simulation is the full effect of the varied hydrogen bonding environment. The nonrephasing spectrum for the unencapsulated Nile red in the pure solvent mixture in Figure 2(c) shows small splitting of peak B, as does that for the unencapsulated peak B in the dilute phase in Figure 2(g). The nonrephasing spectrum for the unencapsulated Nile red in Figure 5(a) more clearly shows that B splits into two peaks at (1587,1583) cm^{-1} and (1589,1594) cm^{-1} around T_w = 0.6 ps. The intensity of the peak observed at (1587,1583) cm^{-1} decreases until only one peak is observed at about 1.3

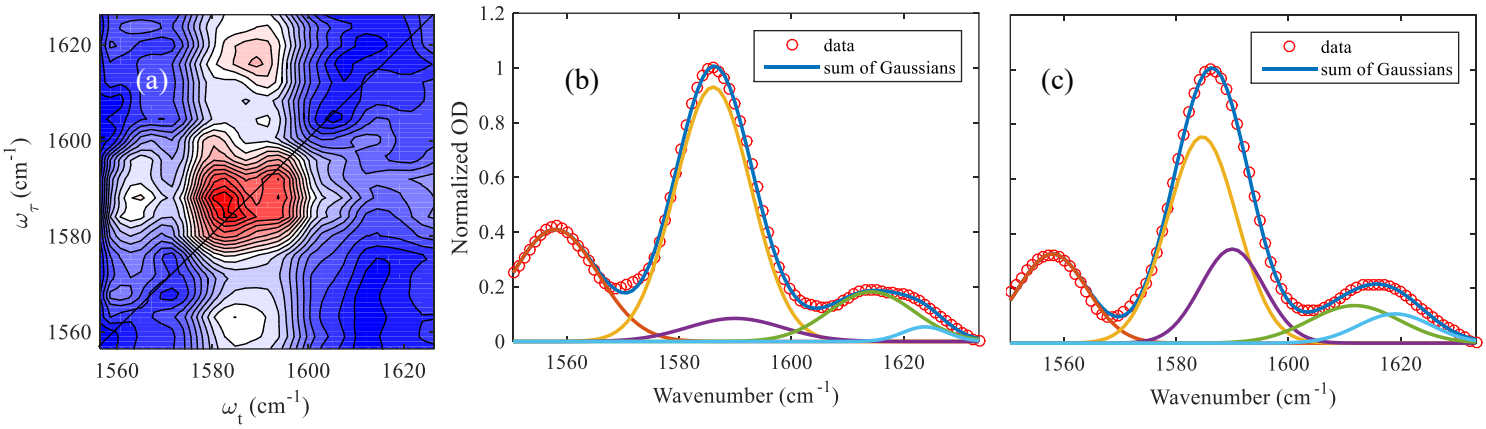

Figure 5: (a) Absolute value nonrephasing 2D IR spectrum of Nile red in 30% D_2O and 70% dioxane at T_w = 0.6 ps. (b) and (c) are the FTIR spectra of Nile red in dioxane–D_2O with 25% and 30% D_2O, respectively, with five Gaussian fits.

ps. It is challenging to characterize the relative intensities of the peaks separately due to significant overlap, but it appears that the lower frequency peak decays with a constant of about 0.75 ps. We expect that the unencapsulated Nile red in the solution with the polymer would have the same behavior. In contrast, the encapsulated Nile red peak does not appear to show this splitting, indicating greater uniformity, although this is hard to confirm, as the unencapsulated and encapsulated Nile red peaks are only separate at waiting times equal to or less than 0.3 ps in the acquired data and slightly earlier in the simulation.

The time-dependent two-peak feature observed in the unencapsulated Nile red is most likely from a combination of two sources. First, hydrogen bonding splits the frequency. Next, energy transfer to nearby modes A and C causes the two peaks to fluctuate in intensity in challenging-to-simulate ways. Nile red in 70% dioxane and 30% D_2O can form hydrogen bonds with D_2O. This would likely cause a shift in the frequency. It is challenging to acquire FTIR spectra of Nile red with no hydrogen bonding possible. While pure dioxane may not form hydrogen bonds with Nile red, it is challenging to obtain pure dioxane, without alcohol stabilizers, because it is a peroxide former. Alternatively, dry solvents were considered, but we realized that the solid Nile red we had already contained some H_2O in it. Instead, we focused on obtaining spectra with varying volumes of D_2O. When doing so, we observed that the FTIR

spectra acquired in this region could best be fit by the sum of five Gaussians, as shown in Figure 5(b) and 5(c). Mode A does not appear to shift in frequency when the percentage of D_2O in dioxane increases from 25% to 30% by volume. Modes B and C appear to slightly blue-shift in frequency with increasing D_2O concentration because their underlying higher-frequency components become relatively stronger than the lower-frequency components. This behavior was not expected, as carbonyl modes typically decrease in frequency when hydrogen bonded.[64] We attribute the difference here to several factors. Most importantly, modes B and C come from more than just the carbonyl stretching. Both have significant contributions from other bonds in the molecule. The presence of the hydrogen bond likely changes the coupling between the three modes (as well as the many other modes in the molecule), which may then reduce (or increase) the coupling, resulting in a complicated-to-predict effect on the frequency of the hydrogen-bonded compared to the free Nile red. Finally, hydrogen bonding preference between O···HO and π···HO can differ by less than 1 kJ/mol, lower than the thermal energy at ambient temperature.[65] The existence of the other prominent resonance structure of Nile red[58] [Figure 1(a) bottom] may change the preference for O···HO compared to π···HO because the C=O bond involved in modes A, B, and C will have a bond order between 1 and 2. While O···HO is typically more energetically favorable, it is possible that the interaction with two aromatic moieties may tip the scale to favor π···HO,[66] which may give rise to the unexpected frequency shifts we observed. The reasonably good agreement between the FTIR difference in frequency, ~6.8 cm^{-1}, and the difference in frequency between the two peaks in the nonrephasing spectrum, 9–11 cm^{-1}, depending on the waiting time, indicates that this is the most likely explanation for this time dependent two-peak feature. Recall that the frequency separation in the nonrephasing is likely to be larger due to the presence of the nodal plane between the two peaks.[22]

Conclusions

Solutions of Nile red in dioxane–D_2O with and without PEG_{45}-*b*-PCL_{30} were measured to determine the percent encapsulation in the polymer droplets and to characterize this encapsulation. Pump–

probe data acquired confirmed that the lifetime of the encapsulated Nile red is longer than that of the unencapsulated Nile red. Furthermore, the Fourier transformation of the lifetime residuals shows that the frequency shift caused by encapsulation is ~4–6 cm^{-1}. The dynamics of unencapsulated and encapsulated Nile red were characterized by waiting-time-dependent 2D IR. The time evolution of CLS was extracted for both species to visualize the dynamics, despite the significant coupling among vibrators. Strong agreement between simulated and experimental 2D IR spectra and dynamics increased confidence in the parameters determined to describe the unencapsulated and encapsulated Nile red. Based on the increased lifetime for encapsulated Nile red, the encapsulated Nile red is likely more shielded from the solvent electric field by the polymer droplets. This is consistent with encapsulation in a coacervate microdroplet. The large oscillatory features observed in the CLS for both the encapsulated and unencapsulated Nile red were successfully recovered in the simulation, indicating that they likely predominantly arise from coupling between the three modes investigated. This also allowed us to confirm the dynamics for other modes, as the magnitude of these oscillatory features depends significantly on the parameters chosen for the other two modes. The oscillatory feature in the lifetime data was also recovered in the simulation, confirming the two origins. First, the coupling between B and A as well as B and C, and second, the interference between the encapsulated and unencapsulated Nile red signal when polymer was present. The larger Gaussian width and faster rate in the vibrational spectral diffusion dynamics of encapsulated Nile red, compared to unencapsulated Nile red, are attributed to the different solvent and local polymer environments, which Nile red preferentially absorbed at the PEG-PCL interface would experience in coacervate microdroplets with internal nanoscale structures. This study demonstrates that 2D IR spectroscopy (with scattering removal) is effective in characterizing the complex dynamics of unencapsulated and encapsulated small molecules and revealing molecular environment within polymer (micro)droplets. Future study may include probing how small molecules interact with polymer droplets, which may be important in selecting the most effective polymers for particular uses.[67]

Acknowledgements

This paper is based on a study supported by the National Science Foundation (Grant No. CHE-1905395) and the National Institute of Health (Grant No. R21EB034418). Any opinions, findings, and conclusions or recommendations expressed in this paper are those of the authors and do not necessarily reflect the views of the National Science Foundation or the National Institute of Health. A.M.C. acknowledges the support of the Rose Hills Foundation through fellowships. We would also like to acknowledge UCI Greenplanet and NSF Grant No. CHE-0840513 for the computations performed on their cluster. We acknowledge UCI Laser Spectroscopy Labs. We would also like to acknowledge Hiroaki Maekawa for laser maintenance and fruitful discussions.

AUTHOR DECLARATIONS

Conflict of Interest

The authors have no conflicts to disclose.

Author Contributions

A.M.C. performed linear and 2D IR experiments, data analysis, and simulation. V.W. performed DFT calculations. N.S.I. and J.P.P. provided samples and discussions. N.S.I. collected supporting FTIR spectra. A.M.C. and N.-H.G. discussed the data and wrote the paper. N.-H.G. planned and conceptualized the study.

Anneka Miller Casas: Data curation (lead); Formal analysis (lead); Investigation (lead); Methodology (equal); Software (lead); Validation (lead); Visualization (lead); Writing – original draft (lead); Writing – review & editing (supporting). **Victor Wen:** Formal analysis (supporting); Visualization (supporting). **Nehal S. Idris:** Investigation (supporting); Resources (equal). Joseph **P. Patterson:** Resources (equal). **Nien-Hui Ge:** Conceptualization (lead); Funding acquisition (lead); Methodology (equal); Resources (lead); Supervision (lead); Visualization (supporting); Writing – original draft (supporting); Writing – review & editing (lead).

DATA AVAILABILITY

The data that support the findings of this study are available from the corresponding author upon reasonable request.

References

[1] J. R. Jambeck, R. Geyer, C. Wilcox, T. R. Siegler, M. Perryman, A. Andrady, R. Narayan, and K. L. Law, "Plastic waste inputs from land into the ocean," *Science* **347**, 768 (2015).

[2] A. A. Koelmans, N. H. M. Nor, E. Hermsen, M. Kooi, S. M. Mintenig, and J. D. France, "Microplastics in freshwaters and drinking water: Critical review and assessment of data quality," *Water Research* **155**, 410 (2019).

[3] M. C. Rillig, "Microplastic in Terrestrial Ecosystems and the Soil," *Environ. Sci. Technol.* **46**, 6453 (2012).

[4] Y. Deng, S. Schafer, D. Kronstein, A. Atabay, M. Susewind, E. Krieg, S. Seiffert, and J. Gaitzsch, "Amphiphilic Block Copolymers PEG-*b*-PMTCs: Synthesis, Self-Assembly, Degradation Properties and Biocompatibility," *Biomacromolecules* **25**, 303 (2024).

[5] D. A. Wood, "Biodegradable drug delivery systems," *International Journal of Pharmaceutics* **7**, 1 (1980).

[6] C. A. Bader, E. A. Carter, A. Safitri, P. V. Simpson, P. Wright, S. Stagni, M. Massi, P. A. Lay, D. A. Brooks, and S. E. Plush, "Unprecedented staining of polar lipids by a luminescent rhenium complex revealed by FTIR microspectroscopy in adipocytes," *Mol. BioSyst.* **12**, 2064 (2016).

[7] P. Greenspan, E. P. Mayer, and S. D. Fowler, "Nile Red: A Selective Fluorescent Stain for Intracellular Lipid Droplets," *J. Cell Biol* **100**, 965 (1985).

[8] P. Hazra, D. Chakrabarty, A. Chakraborty, and N. Sarkar, "Intramolecular Charge Transfer and Solvation Dynamics of Nile Red in the Nanocavity of Cyclodextrins," *Chem. Phys. Lett.* **388**, 150 (2004).

[9] A. Ray, S. Das, and N. Chattopadhyay, "Aggregation of Nile Red in Water: Prevention through Encapsulation in β-Cyclodextrin," *ACS Omega* **4**, 15 (2019).

[10] C. Martin, S. Bhattacharyya, A. Patra, and A. Douhal, "Single and Multistep Energy Transfer Processes within Doped Polymer Nanoparticles," *Photochem. Photobiol. Sci.* **13**, 1241 (2014).

[11] C. Martín, M. R. di Nunzio, B. Cohen, and A. Douhal, " Location and Freedom of Single and Double Guest in Dye-Doped Polymer Nanoparticles," *Photochemical & photobiological sciences : Official journal of the European Photochemistry Association and the European Society for Photobiology* **13**, 1580 (2014).

[12] N. C. Maitia, M. M. G. Krishna, P. J. Britto, and N. Periasamy, "Fluorescence Dynamics of Dye Probes in Micelles," *The journal of physical chemistry. B* **101**, 9 (1997).

[13] A. Datta, D. Mandal, S. K. Pal, and K. Bhattacharyya, "Intramolecular Charge Transfer Processes in Confined Systems. Nile Red in Reverse Micelles," *The journal of physical chemistry. B* **101**, 10221 (1997).

[14] A. P. Goodwin, J. L. Mynar, Y. Ma, G. R. Fleming, and J. M. J. Frechet, "Synthetic Micelle Sensitive to IR Light via a Two-photon Process," *J. Am. Chem. Soc.* **127**, 9952 (2005).

[15] A. M. Casas, N. S. Idris, V. Wen, J. P. Patterson, and N.-H. Ge, "Scattering Elimination in 2D IR Immune from Detector Artifacts " *The journal of physical chemistry. B* **128**, 8835 (2024).

[16] P. Hamm and M. T. Zanni. *Concepts and Methods of 2D Infrared Spectroscopy*; Cambridge University Press, 2011.

[17] P. Hamm, M. Lim, and R. M. Hochstrasser, "Structure of the Amide I Band of Peptides Measured by Femtosecond Nonlinear-Infrared Spectroscopy," *The Journal of Physical Chemistry B* **102**, 6123 (1998).

[18] M. C. Asplund, M. T. Zanni, and R. M. Hochstrasser, "Two-dimensional infrared spectroscopy of peptides by phase-controlled femtosecond vibrational photon echoes," *Proc Natl Acad Sci USA* **97**, 8219 (2000).
[19] S. Woutersen and P. Hamm, "Structure determination of trialanine in water using polarization sensitive two-dimensional vibrational spectroscopy," *J. Phys. Chem. B* **104**, 11316 (2000).
[20] M. T. Zanni, S. Gnanakaran, J. Stenger, and R. M. Hochstrasser, "Heterodyned two-dimensional infrared spectroscopy of solvent-dependent conformations of acetylproline-NH2.," *J. Phys. Chem. B* **105**, 6520 (2001).
[21] O. Golonzka and A. Tokmakoff, "Polarization-selective third-order spectroscopy of coupled vibronic states," *J. Chem. Phys.* **115**, 297 (2001).
[22] N.-H. Ge, M. T. Zanni, and R. M. Hochstrasser, "Effects of Vibrational Frequency Correlations on Two-Dimensional Infrared Spectra," *J. Phys. Chem. A* **106**, 962 (2002).
[23] N. Demirdoven, M. Khalil, and A. Tokmakoff, "Correlated Vibrational Dynamics Revealed by Two-Dimensional Infrared Spectroscopy," *Physical Review Letters* **89**, 237401 (2002).
[24] M. Khalil, N. Demirdoven, and A. Tokmakoff, "Coherent 2D IR Spectroscopy: Molecular Structure and Dynamics in Solution," *J. Phys. Chem. A* **107**, 5258 (2003).
[25] Y. S. Kim and R. M. Hochstrasser, "Chemical exchange 2D IR of hydrogen-bond making and breaking," *Proceedings of the National Academy of Sciences* **102**, 11185 (2005).
[26] E. E. Fenn and M. D. Fayer, "Extracting 2D IR frequency-frequency correlation functions from two component systems," *J Chem Phys* **135**, 074502 (2011).
[27] J. Nishida, A. Tamimi, H. Fei, S. Pullen, S. Ott, S. M. Cohen, and M. D. Fayer, "Structural dynamics inside a functionalized metal–organic framework probed by ultrafast 2D IR spectroscopy," *PNAS* **111**, 18442 (2014).
[28] N. S. Idris, M. Naseer, J. T. Mulvey, A. Rizvi, N. A. T. Nguyen, and J. P. Patterson, "Understanding the Encapsulation Behavior of Nile Red within Nonionic Block Copolymer Coacervates and Self-Assembled Particles," *Macromolecules* **59**, 1307 (2026).
[29] I. Vinogradov, Y. Feng, S. K. Karthick Kumar, C. Guo, N. S. Udagawa, and N.-H. Ge, "Ultrafast vibrational dynamics of the tyrosine ring mode and its application to enkephalin insertion into phospholipid membranes as probed by two-dimensional infrared spectroscopy," *Journal of Chemical Physics* **155**, 035102 (2021).
[30] Y. Feng, I. Vinogradov, and N.-H. Ge, "General noise suppression scheme with reference detection in heterodyne nonlinear spectroscopy," *Opt. Express* **25**, 26262 (2017).
[31] Y. Feng, I. Vinogradov, and N.-H. Ge, "Optimized noise reduction scheme for heterodyne spectroscopy using array detectors," *Opt. Express* **27**, 20323 (2019).
[32] P. M. Donaldson, Hawkins, A.P., Howe, R.F., "Distinctive signatures and ultrafast dynamics of Bronsted sites, silanol nests and adsorbed water in zeolites revealed by 2D-IR spectroscopy " *Chemical Science* **16**, 6688 (2025).
[33] M. J. Frisch, G. W. Trucks, H. B. Schlegel, G. E. Scuseria, M. A. Robb, J. R. Cheeseman, G. Scalmani, V. Barone, G. A. Petersson, H. Nakatsuji, X. Li, M. Caricato, A. V. Marenich, J. Bloino, B. G. Janesko, R. Gomperts, B. Mennucci, H. P. Hratchian, J. V. Ortiz, A. F. Izmaylov, J. L. Sonnenberg, D. Williams-Young, F. Ding, F. Lipparini, F. Egidi, J. Goings, B. Peng, A. Petrone, T. Henderson, D. Ranasinghe, V. G. Zakrzewski, J. Gao, N. Rega, G. Zheng, W. Liang, M. Hada, M. Ehara, K. Toyota, R. Fukuda, J. Hasegawa, M. Ishida, T. Nakajima, Y. Honda, O. Kitao, H. Nakai, T. Vreven, K. Throssell, J. A. J. Montgomery, J. E. Peralta, F. Ogliaro, M. J. Bearpark, J. J. Heyd, E. N. Brothers, K. N. Kudin, V. N. Staroverov, T. A. Keith, R. Kobayashi, J. Normand, K. Raghavachari, A. P. Rendell, J. C. Burant, S. S. Iyengar, J. Tomasi, M. Cossi, J. M. Millam, M. Klene, C. Adamo, R. Cammi, J. W. Ochterski, R. L. Martin, K.

Morokuma, O. Farka, J. B. Foresman, and D. J. Fox. Gaussian 16, Revision A.03; Revision A.03 ed.; Gaussian 16, 2016.

[34] A. M. Casas. Scattering Elimination Immune from Detector Artifacts in Two-Dimensional Infrared Spectroscopy and its Application to Polymers. Ph.D. Dissertation, University of California Irvine, 2024.

[35] J. A. Myers, K. L. M. Lewis, P. F. Tekavec, and J. P. Ogilvie, "Two-color two-dimensional Fourier transform electronic spectroscopy with a pulse-shaper," *Opt. Express* **16**, 17420 (2008).

[36] K. M. Farrell, N. Yang, and M. T. Zanni, "A polarization scheme that resolves cross-peaks with transient absorption and eliminates diagonal peaks in 2D spectroscopy," *PNAS* **119**, e2117398119 (2022).

[37] S. Sul, D. Karaiskaj, Y. Jiang, and N.-H. Ge, "Conformations of *N*-Acetyl-L-Prolinamide by Two-Dimensional Infrared Spectroscopy," *The Journal of Physical Chemistry B* **110**, 19891 (2006).

[38] H. Maekawa, F. Formaggio, C. Toniolo, and N.-H. Ge, "Onset of 3_{10}-Helical Secondary Structure in Aib Oligopeptides Probed by Coherent 2D IR Spectroscopy," *Journal of the American Chemical Society* **130**, 6556 (2008).

[39] H. Maekawa, S. Soohwan, and N.-H. Ge, "Vibrational correlation between conjugated carbonyl and diazo modes studied by single- and dual-frequency two-dimensional infrared spectroscopy," *Chemical Physics* **422**, 22 (2013).

[40] A. Tamimi and M. D. Fayer, "Ionic Liquid Dynamics Measured with 2D IR and IR Pump−Probe Experiments on a Linear Anion and the Influence of Potassium Cations," *J. Phys. Chem. B* **120**, 5842 (2016).

[41] S. A. Yamada, J. Y. Shin, W. H. Thompson, and M. D. Fayer, "Water Dynamics in Nanoporous Silica: Ultrafast Vibrational Spectroscopy and Molecular Dynamics Simulations," *J. Phys. Chem. C* **123**, 5790 (2019).

[42] H. Akaike, "A New Look at the Statistical Model Identification," *IEEE Transactions on Audio, Speech, and Language Processing* **19**, 716 (1974).

[43] D. B. Wong, K. P. Sokolowsky, M. I. El-Barghouthi, E. E. Fenn, C. H. Giammanco, A. L. Sturlaugson, and M. D. Fayer, "Water Dynamics in Water/DMSO Binary Mixtures," *The journal of physical chemistry. B* **116**, 5479 (2012).

[44] K. Heyne, N. Huse, J. Dreyer, E. T. J. Nibbering, T. Elsaesser, and S. Mukamel, "Coherent low-frequency motions of hydrogen bonded acetic acid dimers in the liquid phase," *J. Chem. Phys.* **121**, 902 (2004).

[45] E. T. J. Nibbering and T. Elsaesser, "Ultrafast Vibrational Dynamics of Hydrogen Bonds in the Condensed Phase," *Chem. Rev.* **104**, 1887 (2004).

[46] J. Y. Park, H.-J. Kwon, S. Mondal, H. Han, K. Kwak, and M. Cho, "Two-dimensional IR spectroscopy reveals a hidden Fermi resonance band in the azido stretch spectrum of β-azidoalanine," *Physical chemistry chemical physics : PCCP* **22**, 19223 (2020).

[47] C. T. Middleton, Buchanan, L.E., Dunkelberger, E. B., Zanni, M.T., "Utilizing Lifetimes to Suppress Random Coil Featurers in 2D IR Spectra of Peptides," *The Journal of Physical Chemistry Letters* **2**, 2357 (2011).

[48] P. A. Kocheril, Wang, H., Lee, D., Naji, N., Wei, L., "Nitrile Vibrational Lifetimes as Probes of Local Electric Fields," *The Journal of Physical Chemistry Letters* **15**, 5306 (2024).

[49] S. Kim, Y. Shi, J. Y. Kim, K. Park, and J.-X. Cheng, "Overcoming the barriers in micellar drug delivery: loading efficiency, in vivo stability, and micelle–cell interaction," *Expert Opinion on Drug Delivery* **7**, 49 (2010).

[50] M. Ghezzi, Pescina, S., Padula, C., Santi, P., Del Favero, E., Cantu, L., Nicoli, S., "Polymeric micelles in drug delivery: An insight of the techniques for their characterization and assessment in biorelevant conditions," *Journal of Controlled Release* **332**, 312 (2021).
[51] A. Ianiro, H. Wu, M. M. J. van Rijt, M. P. Vena, A. D. A. Keizer, A. C. C. Esteves, R. Tuinier, H. Friedrich, N. A. J. M. Sommerdijk, and J. P. Patterson, "Liquid–liquid phase separation during amphiphilic self-assembly," *Nature chemistry* **11**, 320 (2019).
[52] J. D. Hybl, A. Yu, D. A. Farrow, and D. M. Jonas, "Polar Solvation Dynamics in the Femtosecond Evolution of Two-Dimensional FourierTransform Spectra," *J. Phys. Chem. A* **106**, 7651 (2002).
[53] K. Kwak, S. Park, I. J. Finkelstein, and M. D. Fayer, "Frequency-frequency correlation functions and apodization in two-dimensional infrared vibrational echo spectroscopy: A new approach," *J. Chem. Phys.* **127**, 124503 (2007).
[54] K. C. Robben and C. M. Cheatum, "Least-Squares Fitting of Multidimensional Spectra to Kubo Line-Shape Models," *J. Phys. Chem. B* **125**, 12876 (2021).
[55] C. Xu and C. R. Baiz, "Cutting through the Noise: Extracting Dynamics from Ultrafast Spectra Using Dynamic Mode Decomposition," *J. Phys. Chem. A* **127**, 9853 (2023).
[56] R. M. Hochstrasser, "Two-dimensional IR-spectroscopy: polarization anisotropy effects," *Chemical Physics* **266**, 273 (2001).
[57] M. C. Asplund, M. Lim, and R. M. Hochstrasser, "Erratum to: “Spectrally resolved three pulse photon echoes in the vibrational infrared” [Chem. Phys. Lett. 323 (2000) 269–277]," *Chemical Physics Letters* **340**, 611 (2001).
[58] M. Marazzi, Gattuso, H., Monari, A., "Nile blue and Nile red optical properties predicted by TD-DFT and CASPT2 methods: static and dynamic solvent effects," *Theor. Chem. Acc.* **135**, 57 (2016).
[59] A. Rizvi, A. Ianiro, P. J. Hurst, J. G. Merham, and J. P. Patterson, "Nonionic Block Copolymer Coacervates," *Macromolecules* **53**, 6078 (2020).
[60] A. Ianiro, Á. González García, S. Wijker, J. P. Patterson, A. C. C. Esteves, and R. Tuinier, "Controlling the Spatial Distribution of Solubilized Compounds within Copolymer Micelles," *Langmuir* **35**, 4776 (2019).
[61] A. Rizvi, B. Favetta, N. Jaber, Y.-K. Lee, J. Jiang, N. S. Idris, B. S. Schuster, W. Dai, and J. P. Patterson, "Revealing nanoscale structure and interfaces of protein and polymer condensates via cryo-electron microscopy," *Nanoscale* **16**, 16706 (2024).
[62] N. S. Vrandečić, M. Erceg, M. Jakić, and I. Klarić, "Kinetic analysis of thermal degradation of poly(ethylene glycol) and poly(ethylene oxide)s of different molecular weight," *Thermochimica Acta* **498**, 71 (2010).
[63] T. Elzein, M. Nasser-Eddine, C. Delaite, S. Bistac, and P. Dumas, "FTIR study of polycaprolactone chain organization at interfaces," *Journal of Colloid and Interface Science* **273**, 381 (2004).
[64] A. Blume, Hubner, W., Messner, G., "Fourier Transform Infrared Spectroscopy of 13C=O labeled Phospholipids Hydrogen Bonding to Carbonyl Groups," *Biochemistry* **27**, 8239 (1988).
[65] H. C. Gottschalk, Altnoder, J., Heger, M., Suhm, M.A., "Control over the Hydrogen-Bond Docking Site in Anisole by Ring Methylation," *Angewandte Chemie International Edition* **55**, 1921 (2015).
[66] C. Medcraft, Zinn, S., Schnell, M., Poblotzki, A., Altnoder, J., Heger, M., Suhm, M.A., Bernhard, D., Stamm, A., Dietrich, F., Gerhards, M., , "Aromatic embedding wins over classical hydrogen bonding – a multi-spectroscopic approach for the diphenyl ether–methanol complex," *Physical Chemistry Chemical Physics* **18**, 25975 (2016).
[67] S. K. Prajapati, A. Jain, A. Jain, and S. Jain, "Biodegradable polymers and constructs: A novel approach in drug delivery," *European Polymer Journal* **120**, 109191 (2019).